Research Paper

The role of clay minerals in the concentration and distribution of critical metals in lateritic palaeosols from NE Iberia

Elisa Laita [*], Blanca Bauluz, Alfonso Yuste

IUCA-Department of Earth Sciences, Faculty of Sciences, Universidad de Zaragoza, Pedro Cerbuna 12, 50009 Zaragoza, Spain

ARTICLE INFO

ABSTRACT

The intense chemical weathering processes that lead to the formation of laterites and bauxites result in the enrichment of critical metals (Sc, V, Co, Ga, Ge, Nb, In, Hf, Ta, W, and REEs), which are of great economic interest and are directly involved in the manufacture of various devices essential for the technology transition. This work focuses on combined geochemical and scanning transmission electron microscopy (STEM) studies of lateritic palaeosols developed in continental profiles (Lower Cretaceous, NE Iberia) in order to evaluate the distribution and concentration of critical metals and their possible relationship with weathering processes. In this study, we show that during the process of laterization the highest weathering produces the highest critical metal concentrations (reaching concentrations of 1914.80 ppm in the lateritic palaeosols and 926.30 ppm in the ferruginous macropisoids). Concentrations normalized to the upper continental crust (Taylor and McLennan, 1985) indicate that both the lateritic palaeosols and the macropisoids are enriched in LREEs (256.81 and 223.01 ppm, respectively) and HREEs (107.11and 110.53, respectively). In the lateritic palaeosols, the (La/Sm)c values are higher than those of (Gd/Yb)c, indicating that the LREEs exhibit higher fractionation with weathering, whereas the opposite occurs for the macropisoids, in which the HREEs have higher fractionation. These data indicate that the HREEs are less mobile than the LREEs during laterization. The critical metals present a good positive correlation with Fe, Ti, and Al, but a good negative correlation with K. STEM images and EDS analyses allowed us to identify REE-phases (including monazite, xenotime, and La, Ce and Nd oxides) and nanoparticles of gold adsorbed on the surface of kaolinite crystals. This shows not only that during the laterization process Fe and Ti oxides act as scavengers for the critical metals, but also that kaolinite controls their distribution.

1. Introduction

Modern society's growing need for raw materials to face its technological needs is expanding the range of metals used in various industries. Special attention is now focused on critical metals, i.e., those metals whose economic importance is gradually increasing, but whose supply may undergo fluctuations due to economic or political factors, making them susceptible to shortages in the future (Gunn, 2014; Chakhmouradian et al., 2015).

The latest report on critical raw materials for the European Union (European Commission, 2023) includes the rare earth elements (REEs), Sc, V, Co, Ga, Sr, Nb, Hf and Ta, as critical metals. These metals are crucial in the green energy, aerospace, medical, automotive, and electronic industries. Within these industries they have numerous applications, in many cases related to the manufacture of components involved in the generation of renewable energies and the production of non-

polluting vehicles, as well as several devices essential for the technology transition (Linnen et al., 2014; Reinhardt et al., 2018).

The intense chemical weathering processes that lead to the formation of aluminium-rich rocks (e.g., laterites and bauxites) can produce enrichment in relatively immobile elements such as REEs, Nb and Ga, among others (Gunn, 2014; Yuste et al., 2017; Yang, M. et al., 2019, Yang, S. et al., 2019). For this reason, considerable attention has recently been paid to laterites and bauxites as potential sources of critical metals, since they can contain critical metal concentrations of economic interest (Gunn, 2014; Yuste et al., 2017; Yang, M. et al., 2019, Yang, S. et al., 2019). However, the abundance of these elements will depend on the palaeogeography, bedrock, climate, drainage, and the pH and redox conditions that prevailed during the formation of these rocks (Mongelli et al., 2017). Variations in the content of critical metals can also occur between deposits of the same age and even within the same deposit, both horizontally and vertically (Mameli et al., 2007; Yuste

et al., 2017; Yuste et al., 2020).

Usually, most of the critical metals are correlated with the Al content, with aluminium hydroxides and kaolinite controlling their distribution (Abedini et al., 2022; Mongelli et al., 2021). Some authors link REEs to detrital phases inherited from the parent rock (Maksimovic and Pantó, 1991), while others suggest that REEs can be adsorbed on mineral surfaces in the form of ions (Linnen et al., 2014). Furthermore, REE fractionation during weathering can also take place through the formation of authigenic REE minerals (Maksimovic and Pantó, 1991). Undoubtedly, research into the minerals hosting the critical metals in laterites and bauxites is essential for designing effective extraction strategies in the future. However, detailed research into clay-minerals to infer their role in the accumulation of critical metals is still lacking. Therefore, this work aims to conduct geochemical analysis in conjunction with a scanning transmission electron microscopy (STEM) study of lateritic palaeosols. The research has two main goals: 1) to evaluate the concentration of major, minor and trace elements in the different lateritic levels and ferruginous macropisoids and their relationship with the intensity of the weathering; and 2) to determine what form the critical metals take in the lateritic palaeosols, and the role of clay minerals in the distribution of these metals within the lateritic levels and the ferruginous macropisoids.

2. Description of the palaeosol samples

The samples come from palaeosols that developed on four Lower Cretaceous (early Barremian) continental profiles (ALC, VE, JO, and EST) located in the SE part of the Iberian Range (NE Iberia) (Fig. 1a). A previous characterization of these materials by X-ray diffraction (XRD), optical microscopy, field emission scanning electron microscopy (FESEM), and energy-dispersive analyses was performed by Laita et al. (2020).

According to our previous work, the palaeosols can be classified as laterites and they developed in situ through the chemical weathering of lacustrine mudstones and marlstones. The lower levels of the profiles are formed of red clays (RC) containing abundant ferruginous pisoids and macropisoids, whereas the middle and upper levels correspond to ochre and violet clays/marls (OVC) with few or no pisoids (Fig. 1b and c).

The mineralogical composition of the lateritic palaeosols reported by Laita et al. (2020) can be found in the Supplementary Materials (Fig. S1 and Table S1). The palaeosols are composed of calcite, quartz, clay minerals, hematite, goethite, orthoclase, anatase, rutile, ilmenite, and diaspore. The RC samples contain abundant kaolinite, whereas kaolinite, smectite (beidellite-type), illite and illite/smectite mixed layers are identified in the OVC. The macropisoids are formed of

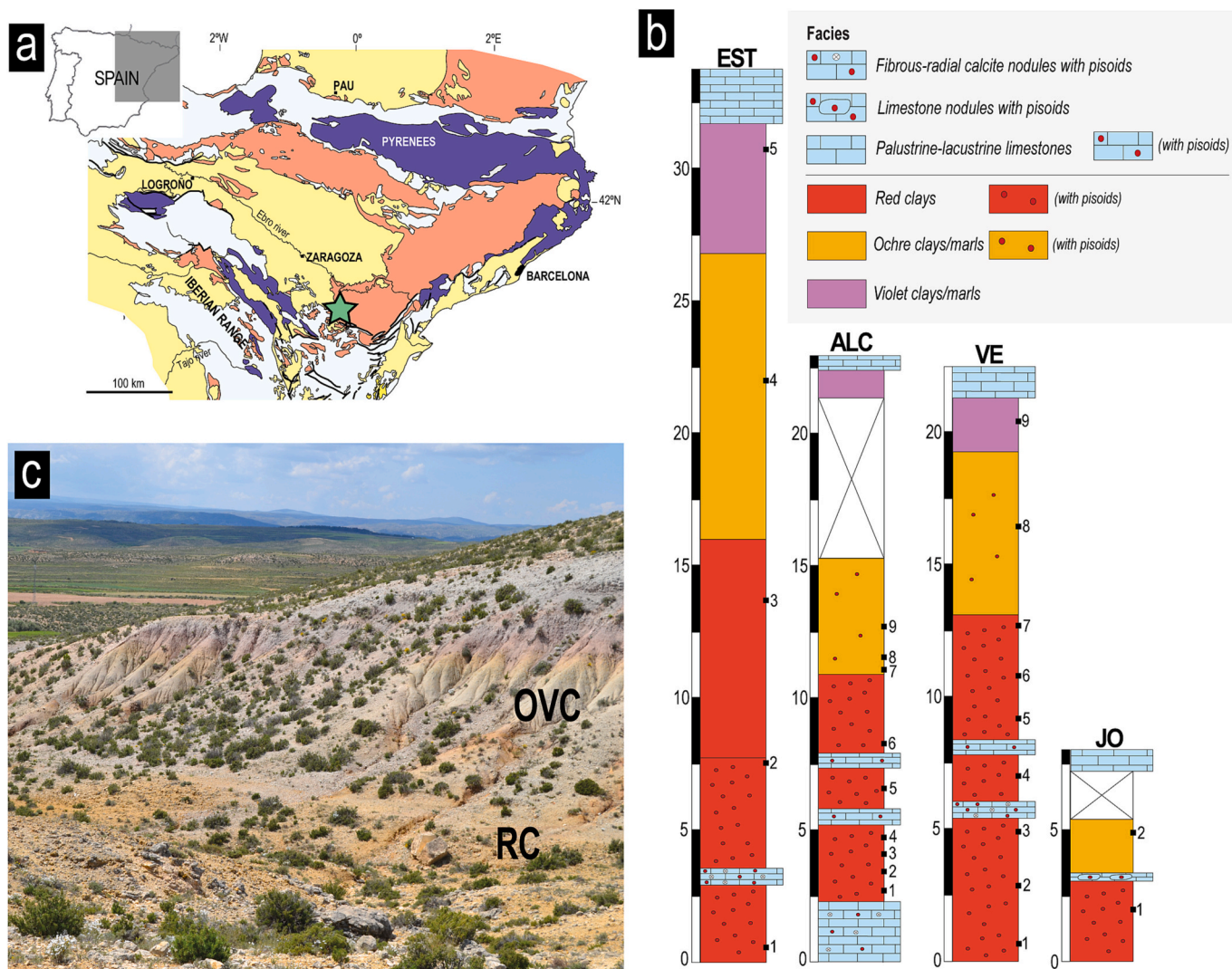**Fig. 1.** a) Simplified geological map of the NE Iberian Peninsula including the location of the studied profiles (green star), b) the four stratigraphic profiles including sample location, c) field view of the red clays (RC) and the ochre and violet clays/marls (OVC). Modified from Laita et al. (2020). (For interpretation of the references to colour in this figure legend, the reader is referred to the web version of this article.)

hematite, goethite, ilmenite, quartz, calcite, and kaolinite (deduced by FESEM analyses) (Fig. S1, Table S1). FESEM images are included in the Supplementary Materials (Fig. S2). The images revealed the authigenic origin of kaolinite and beidellite, as well as the detrital origin of illite and quartz. No evidence of halloysite and/or amorphous phases were detected (Laita et al., 2020). The matrix of the RC and the OVC was cemented by microsparite and sparite during the early diagenesis (see Fig. S2c and d). This diagenesis could also generate micritic nodules and sparitic-microsparitic intraclasts that are observed in the OVC (Laita et al., 2020). Therefore, calcite in the palaeosols has a diagenetic origin, but this diagenesis did not alter the authigenic clay minerals (Laita et al., 2020).

An upward decrease in the authigenic kaolinite and pisoid contents towards the top of the profiles, coinciding with an increase in detrital quartz and illite and the presence of authigenic beidellite, reflects a decrease in the chemical weathering intensity related to a change from warm and humid to cooler and drier conditions (Laita et al., 2020, 2023).

3. Methods

A total of 30 samples from different lateritic levels included in the four profiles described by Laita et al. (2020) were selected for this study: 17 correspond to red clays (RC), 8 to ochre and violet clays/marls (OVC), and 5 to macropisoids (Fig. 1).

Chemical analyses of major and trace elements in bulk samples were performed at Actlabs Laboratories (Canada). Major elements and some trace elements (V, Sr, Ba, Sc, Be) were determined by inductively coupled plasma optical emission spectroscopy (ICP-OES). Fused samples (lithium metaborate/tetraborate fusion) were rapidly digested in a weak nitric acid and run on a combination of simultaneous/sequential Thermo Jarrell-Ash ENVIRO II ICP or a Varian Vista 735 ICP. Calibration was performed using seven prepared USGS- and CANMET-certified reference materials (see Table S2 in the Supplementary Materials). One of the seven standards was used during the analysis for every group of ten samples. The detection limit for the major elements was 0.01% (except for MnO and TiO_2 with detection limits of 0.001%).

The rest of the trace elements were analysed by inductively coupled plasma mass spectrometry (ICP-MS). Fused samples were diluted and analysed by a Perkin Elmer Sciex ELAN 6000, 6100, or 9000 ICP-MS. Three blanks and five controls were analysed per group of samples. Duplicates were fused and analysed every 15 samples. The detection limit for each trace element is indicated in brackets: Cr and Ni (20 ppm), Co, Rb, and Zr (1 ppm), Y (0.5 ppm), Nb (0.2 ppm), Cs and Hf (0.1 ppm), Th, La, Ce, and Nd (0.05 ppm), U, Pr, Sm, Gd, Tb, Dy, Ho, Er, and Yb (0.01 ppm), Lu (0.002 ppm), and Eu and Tm (0.005 ppm).

The micritic nodules and sparitic-microsparitic intraclasts included in the OVC (Laita et al., 2020) may be causing the content of CaO of the OVC samples to be higher (Table 1). Nevertheless, as mentioned above, the carbonate in the lateritic samples has a diagenetic origin and thus, it does not have a genetic relationship with the lateritic palaeosols (Laita et al., 2020), so the CaO values obtained by ICP-OES are reported for each sample but are not considered in this study.

Major and trace elements have been normalized by Upper Continental Crust values (UCC) of Taylor and McLennan (1985). Trace elements have also been normalized by chondrite values of Taylor and McLennan (1985). When values are normalized to the UCC, the subscript N is used, whereas the subscript c is used for those values normalized to chondrite (e.g., (La/Sm)c).

To evaluate the degree of chemical weathering within the samples, the chemical index of alteration (CIA) and the Weathering Index of Parker (WIP) were calculated. The Index of Compositional Variability (ICV) was also determined to measure the abundance of alumina relative to other major cations in the samples (see Table S3 in the Supplementary Materials).

The CIA and WIP index were calculated by adapting the formulae proposed by Nesbitt and Young (1982) and Parker (1970), respectively, using molecular proportions of the following oxides: CIA = Al_2O_3/(Al_2O_3 + Na_2O + K_2O) * 100 and WIP = ((2*Na_2O/0.35) + (MgO/0.9) + (2*K_2O/0.25) + (CaO/0.7)) * 100. The ICV was calculated by adapting the formula of Cox et al. (1995): ICV = (Fe_2O_3 + K_2O + Na_2O + CaO + MgO + MnO + TiO_2)/Al_2O_3.

Using the software systat13, two correlation matrices were obtained for the mineralogical and geochemical data for the red clays plus the ochre and violet clays/marls ($n = 25$), as well as for all the clays (RC + OVC) and the macropisoids together ($n = 30$). For the correlation matrix of the red clays and the ochre and violet clays/marls (n = 25), the correlation coefficients show a significance level of 0.01 for $r = 0.49$ and of 0.001 for $r = 0.60$. For the correlation matrix of all the clays and the macropisoids together (n = 30), the correlation coefficients show a significant level of 0.01 for $r = 0.45$ and of 0.001 for $r = 0.55$.

In order to determine how the critical metals are in the lateritic palaeosols and the role of clay minerals in their distribution, six red clays (those with a higher critical metal content) were analysed by scanning transmission electron microscopy (STEM). The study was performed using a F30 TEM, using a HADDF detector and equipped with an energy-dispersive spectroscopy (EDS) system in the Advanced Microscopy Laboratory of the University of Zaragoza, Spain. The accelerating voltage was 300 kV with a beam current of 92 uA. For this study, <53 µm fractions of the samples were extracted. With these samples, suspensions of clay and pure ethanol were prepared and deposited on carbon-coated copper grids. The images were taken using the scanning mode (STEM), which helped to visualize the phases containing REEs and other metals.

4. Results

4.1. Major element geochemistry

Si, Al, and Fe concentrations account for most of the content in the samples (Table 1). On average, the Si content of the RC and the OVC is quite similar to each other (34.31 and 33.35%, respectively). The Al, Fe, and Ti content decreases from the RC (Al = 20.19%; Fe = 11.81%; Ti = 1.20%) to the OVC (Al = 7.16%; Fe = 3.44%; Ti = 0.56%). By contrast, the OVC present a higher K (1.06%) and Mg (0.79%) content than the RC (K = 0.24% and Mg = 0.37). The macropisoids present quite high Fe content (32.31%) and more than twice as much P content as the clays (macropisoids = 0.17%; RC and OVC = 0.06%).

When the data are normalized to the composition of the UCC, an enrichment in Fe, Mn, and Ti is observed in the RC, the OVC, and the macropisoids (Fig. 2a). The RC are also enriched in Al. In contrast, the OVC are somewhat enriched in Si, and the macropisoids are also enriched in P. All the samples are depleted in Mg, Na, and K, although the impoverishment in Mg and K is less noticeable in the OVC.

According to the Fe_2O_3-Al_2O_3-SiO_2 diagram of Aleva (1994) (Fig. 2b), the RC can be classified as laterites, kaolinites, and ferritic kaolinites, whereas the OVC are classified as ferritic kaolinites and kaolinites.

Plots of the CIA, WIP and ICV values vs. critical metal content in ppm are presented in Fig. 3. The average CIA values of the red clays from the lower levels of the profiles are higher (RC = 99–98) than those of the ochre and violet clays/marls from the middle and upper levels (OVC = 77–90), whereas the opposite occurs with the average WIP values, which are higher in the ochre and violet clays marls (RC = 1–10 and OVC = 6–24) (see also Table S3 in the Supplementary Materials).

The critical metal content is higher when the CIA values are higher and the WIP values are lower (Fig. 3a and b). By contrast, there is not such a clear difference in the average ICV values tendency (RC = 0.20–2.5 and OVC = 0.60–1.10) and no relation with the content of critical metals is observed (Fig. 3c).

Table 1

Chemical composition of the red clays (RC), ochre and violet clays/marls (OVC), and macropisoids. Major elements in weight per cent (wt%) and trace elements in parts per million (ppm). Subscript c = concentrations in ppm normalized by chondrite values of Taylor and McLennan (1985).

Outcrop	Sample clasification	Sample labbel	SiO$_2$	Al$_2$O$_3$	Fe$_2$O$_3$ (T)	MnO	MgO	CaO	Na$_2$O	K$_2$O	TiO$_2$	P$_2$O$_5$	Sc	Be	V	Cr	Co	Ga	Ge	As	Rb	Sr	Zr	Nb	Mo	In	Sn	Sb	Cs	Ba	Hf	Ta	W	∑Critial metals (excluding REEs)
ALC	RC	ALC-1	32.67	25.63	19.65	0.069	0.27	2.66	0.03	0.08	1.204	0.04	28	8	341	170	31	41	2.3	27	5	68	276	24.3	2	0.2	9	3.1	1.8	150	7.4	2.31	4.9	485.51
		ALC-2	37.41	29.13	14.03	0.035	0.28	0.75	0.03	0.14	1.604	0.06	30	8	247	220	21	43	2.3	18	10	74	390	36.3	<2	0.2	11	2.3	3.5	38	10.8	3.13	6.5	402.53
		ALC-3	35.68	27.1	19.49	0.085	0.42	0.62	0.03	0.15	1.618	0.06	34	10	342	200	30	46	2.1	21	12	69	468	36.5	4	0.2	10	3.3	3.6	56	11.9	3.17	7	516.17
		ALC-4	22.8	16.2	19.73	0.045	0.18	17.94	0.02	0.05	0.982	0.05	19	6	339	140	10	29	2.5	23	3	61	262	22.2	2	0.1	7	3.8	1	57	7	1.86	5.6	440.06
		ALC-5	35.39	19.67	2.39	0.051	0.29	17.65	0.03	0.21	1.158	0.05	16	4	50	200	2	21	1.2	<5	10	97	309	25.5	<2	0.1	7	0.9	3.4	44	8.6	2.16	4	131.46
		ALC-6	39.05	8.67	5.03	0.082	0.41	23.23	0.03	0.45	0.696	0.04	11	2	83	160	6	14	0.9	6	15	123	386	14.1	5	<0.1	5	1.1	3.2	35	9.7	1.52	3.1	144.42
	OVC	ALC-7	43.69	6.86	2.54	0.053	0.48	23.89	0.03	0.52	0.65	0.02	8	2	56	140	1	10	0.8	<5	17	134	432	11.4	<2	<0.1	3	1	3.7	45	10.4	1.15	2.9	102.65
		ALC-8	39.82	8.55	3.94	0.043	0.68	23.11	0.02	0.68	0.679	0.03	9	2	73	130	3	13	1	7	23	172	375	13.7	<2	<0.1	3	2.2	5.9	67	9.3	1.28	3.1	128.58
		ALC-9	48	6.84	3.86	0.043	0.7	19.81	0.03	0.93	0.658	0.03	8	2	61	150	3	11	1.2	6	31	160	444	11.6	<2	<0.1	4	2	6.2	216	10.9	1.24	3.2	113.14
VE	RC	VE-1	36.13	27.66	14.52	0.039	0.3	1.64	0.04	0.11	1.575	0.06	28	9	236	190	26	36	2.3	27	8	80	343	31.3	<2	0.2	10	3	2.8	42	9.4	2.91	6.3	381.41
		VE-2	38.72	27.95	2.76	0.014	0.34	8.56	0.04	0.11	1.568	0.05	19	6	60	170	5	25	1.9	<5	8	93	351	34.1	<2	0.1	10	1.6	2.5	77	9.6	2.97	5.8	165.07
		VE-3	42.81	29.23	9.63	0.028	0.43	0.42	0.05	0.15	1.729	0.06	27	8	174	290	26	36	2.7	18	8	105	434	39.3	<2	0.1	11	2.4	2.4	32	11.9	3.32	6.8	329.52
		VE-4	48.55	13.07	4.13	0.04	0.79	13.79	0.03	0.98	0.947	0.05	13	3	59	220	7	17	1.5	<5	30	155	441	20.4	<2	0.1	5	1.5	5.1	34	11.4	1.8	4.1	136.8
		VE-5	27.12	10.44	3.38	0.071	0.52	29.07	0.02	0.31	0.634	0.02	11	2	49	160	2	15	0.9	<5	9	113	265	14.1	<2	<0.1	4	1.1	2.1	22	7	1.17	2.7	103.97
		VE-6	24.9	10.01	3.28	0.062	0.48	29.48	0.02	0.28	0.614	0.04	10	2	55	120	1	14	0.7	<5	8	110	250	13.1	<2	0.1	4	1.1	1.7	25	6.7	1.16	2.7	105.56
		VE-7	35.98	25.64	18.34	0.088	0.38	0.42	0.04	0.11	1.545	0.07	32	9	299	210	43	43	2.7	37	8	89	366	33.9	2	0.2	10	3.5	2.2	68	10.1	2.91	6.6	476.91
	OVC	VE-8	19.87	4.42	1.81	0.065	0.77	37.93	0.03	0.84	0.358	0.04	5	1	38	80	<1	6	0.5	6	25	361	187	7.5	<2	<0.1	2	1.4	2.8	148	4.9	0.61	2.1	66.01
		VE-9	14.5	3.09	1.31	0.063	0.79	41.52	0.04	1.02	0.2	0.07	3	<1	30	40	<1	4	<0.5	<5	29	588	90	3.9	<2	<0.1	1	0.3	2.3	2680	2	0.3	1	44.5
JO	RC	JO-1	32.5	25.96	24.29	0.07	0.37	0.23	0.04	0.2	1.58	0.09	37	8	356	320	14	33	2.6	21	8	116	475	34.7	4	0.2	10	4	2.5	27	12.7	2.76	6.2	503.16
	OVC	JO-2	26.18	8.12	4.45	0.095	1.06	28.78	0.04	1.15	0.575	0.14	10	3	86	110	10	12	0.6	8	50	141	198	12	<2	<0.1	2	0.5	4.8	86	4.7	0.83	1.5	138.13
EST	RC	EST-1	22.45	10.44	24.05	0.325	0.27	17.9	0.03	0.24	0.644	0.1	19	6	197	180	51	21	1.5	68	18	72	197	14.2	<2	0.1	3	1.4	3.1	98	5.1	1.05	3	314.35
		EST-2	29.34	15.16	5.29	0.035	0.24	22.47	0.03	0.31	0.904	0.08	18	3	108	150	12	18	0.9	21	24	90	225	19.8	<2	0.1	4	0.5	4.7	67	6.2	1.49	2.4	187.39
		EST-3	41.75	21.19	10.77	0.056	0.32	6.53	0.04	0.22	1.411	0.07	24	4	186	270	22	29	2.2	24	20	141	355	30	<2	0.1	6	1.3	4.6	90	9.4	2.43	5.7	312.13
	OVC	EST-4	32.98	9.86	5.06	0.084	0.71	23.49	0.04	0.96	0.684	0.08	12	2	97	170	13	13	1	26	52	165	237	14.5	<2	0.1	3	0.7	5.3	178	6	1.05	2	160.35
		EST-5	41.74	9.56	4.52	0.034	1.14	19.33	0.06	2.39	0.708	0.09	10	2	53	160	4	13	1.2	5	100	181	294	14	<2	<0.1	4	1.7	6	145	8	1.22	2.9	109.02
Macropisoids			11.35	4.42	29.15	0.395	0.23	27.24	0.01	0.04	0.318	0.12	14	6	308	90	42	16	1.2	42	2	47	145	7.8	2	0.1	3	5.1	0.5	39	3.6	0.49	4	402.29
			10.12	5.31	25.11	0.359	0.21	30.06	0.02	0.04	0.368	0.09	13	5	259	80	33	16	1	36	1	51	127	8.1	<2	0.1	2	3.5	0.4	35	3	0.6	3.2	340.5
			9.61	2.9	11.17	0.195	0.17	39.26	0.01	0.05	0.21	0.09	8	3	133	70	16	10	0.5	20	2	53	109	5.2	<2	<0.1	2	1.9	0.6	13	2.9	0.3	1.9	179.7
			16.8	4.2	52.34	0.301	0.64	15.68	0.04	0.48	0.24	0.3	8	42	253	120	27	11	0.5	24	18	85	85	4.9	17	0.1	1	3	1.3	392	2.2	0.4	3.7	313.8
			14.6	5.43	43.79	0.492	0.32	14.88	0.02	0.03	0.404	0.26	14	8	444	100	63	19	1.4	70	1	43	179	9.2	7	0.2	3	7.7	0.3	38	4.6	0.67	3.8	567.57

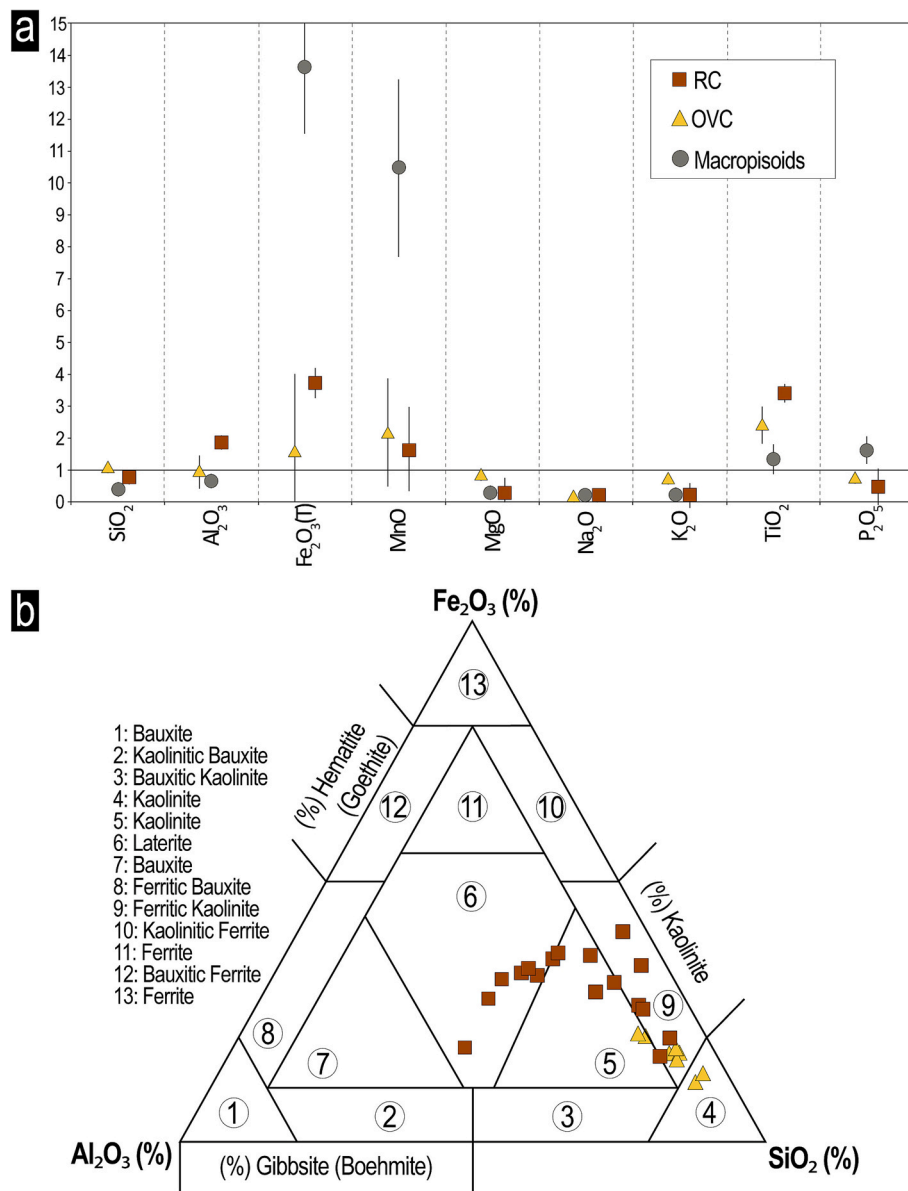| Outcrop	Sample clasification	Sample labbel	Tl	Bi	Th	U	Ni	Cu	Zn	Ag	Pb	Y	La	Ce	Pr	Nd	Sm	Eu	Gd	Tb	Dy	Ho	Er	Tm	Yb	Lu	LOI	∑REE	∑LREE	∑HREE	(La/Sm)c	(Gd/Yb)c	(La/Yb)c	∑Critial metals
ALC	RC	ALC-1	0.18	0.8	23.4	3.21	90	50	160	0.5	42	58.3	39.8	83.8	6.65	24.8	5.32	1.29	6.41	1.17	7.73	1.65	4.73	0.69	4.43	0.677	16.1	247.45	87.08	79.38	4.71	1.17	6.07	732.96
		ALC-2	0.33	0.6	25.9	3.52	80	50	120	1.3	28	90.4	62.8	86.7	9.81	35.1	7.42	1.79	9.69	2	13.1	2.68	8.01	1.15	7.39	1.17	15.61	339.21	201.83	125.90	5.33	1.06	5.74	741.74
		ALC-3	0.38	0.6	26.2	5.15	120	50	180	1.4	39	113	70.8	105	12.7	48.6	10.9	2.67	13.2	2.66	17.6	3.66	11	1.61	10.3	1.6	15.38	425.30	248.00	161.43	4.09	1.04	4.64	941.47
		ALC-4	0.14	1.1	20.6	2.75	50	30	80	0.9	47	67.5	45.8	51.3	7.71	30.1	5.93	1.42	7.36	1.26	7.74	1.6	4.64	0.645	4.15	0.664	22.85	237.82	140.84	88.20	4.86	1.44	7.46	677.88
		ALC-5	0.16	0.3	17.5	2.96	40	20	40	1	14	72.1	72.7	123	13.1	50.4	9.38	2.08	9.44	1.52	8.88	1.81	5.33	0.747	4.75	0.762	23.48	376.00	268.58	95.90	4.88	1.61	10.34	507.46
		ALC-6	0.17	0.2	12.6	2.82	50	30	40	1.2	18	84.6	80.7	102	14.8	59.5	11.6	2.47	11.9	1.84	10.8	2.18	5.97	0.796	4.93	0.793	23.48	394.88	268.60	111.91	4.38	1.96	11.06	539.30
	OVC	ALC-7	0.13	0.2	11.5	2.99	20	20	<30	1.4	11	57.2	53.5	82.6	10.9	42.1	8.41	1.71	8.26	1.38	8	1.58	4.52	0.658	4.15	0.64	22.16	285.61	197.51	78.13	4.00	1.61	8.71	388.26
		ALC-8	0.17	0.3	11.4	2.76	30	<10	<30	1.1	12	54.9	53.4	81.7	10.8	41.9	8.28	1.64	8.02	1.27	7.61	1.46	4.44	0.618	3.95	0.639	23.08	280.63	196.08	74.89	4.06	1.65	9.14	409.21
		ALC-9	0.24	0.1	11.8	2.94	20	10	<30	1.3	9	49.8	50.9	75.1	9.67	37.4	7.08	1.37	7.13	1.13	6.77	1.37	4	0.586	3.72	0.597	19.64	256.62	180.15	67.97	4.53	1.55	9.25	369.76
VE	RC	VE-1	0.27	1.1	23.8	3	90	40	110	0.8	31	99.9	51.6	70.7	7.59	27.9	6.2	1.6	8.66	1.77	12.4	2.67	7.66	1.11	6.76	1.03	16.3	307.55	163.99	133.30	5.24	1.04	5.16	688.96
		VE-2	0.26	0.6	21.6	2.98	40	10	50	1.1	14	93.6	60	101	9.61	36.2	7.23	1.57	8.73	1.68	11.3	2.49	7.42	1.08	6.74	1.01	19.77	349.66	214.04	125.32	5.22	1.05	6.02	514.73
		VE-3	0.25	0.8	27	4.2	100	20	120	1.3	25	148	181	274	35.4	137	25.4	5.3	23	3.53	20.2	3.97	11.8	1.63	10.3	1.52	15.74	882.05	652.80	200.95	4.49	1.81	11.87	1211.57
		VE-4	0.34	0.3	16.3	2.81	30	<10	40	1.4	13	74	66.9	99.2	13.4	50.7	9.51	2	9.76	1.66	9.72	1.96	5.72	0.804	5.1	0.793	18.48	351.23	239.71	99.76	4.43	1.55	8.86	488.03
		VE-5	0.13	0.2	11.2	2.22	30	10	50	0.9	14	55.8	52	75	10.3	39.6	7.92	1.57	7.38	1.2	6.83	1.39	4.09	0.569	3.59	0.531	29.18	267.77	184.82	74.00	4.13	1.67	9.79	371.74
		VE-6	0.07	0.2	10.9	2.49	30	10	50	0.8	13	51.6	49.6	74.3	9.54	37.4	7.3	1.52	7.34	1.16	6.66	1.37	3.87	0.556	3.43	0.536	30.02	256.18	178.14	69.18	4.28	1.73	9.77	361.74
		VE-7	0.23	0.9	25.2	4.1	150	60	190	1.1	33	263	306	395	59.2	238	44.3	9.44	41.9	5.93	32.5	6.45	17.9	2.4	13.8	2.07	16.1	1437.89	1042.50	344.05	4.35	2.46	14.98	1914.80
	OVC	VE-8	0.18	<0.1	7.17	1.84	<20	<10	<30	0.6	8	31.4	31	45.8	6.28	25.1	4.77	0.912	4.66	0.76	4.38	0.85	2.48	0.352	2.27	0.361	33.14	161.38	112.95	42.85	4.09	1.66	9.23	227.39
		VE-9	0.16	<0.1	4.08	0.94	<20	<10	<30	<0.5	<5	18.4	16.5	28.9	3.82	14.7	3.21	0.65	3.06	0.46	2.61	0.51	1.4	0.195	1.28	0.197	35.55	95.89	67.13	25.05	3.24	1.94	8.71	140.39
JO	RC	JO-1	0.35	0.8	27.7	5.8	70	10	80	1.6	69	175	193	195	34.3	135	24.5	5.38	23.1	3.69	21.5	4.22	12	1.65	10.5	1.58	13.16	840.42	581.80	230.14	4.96	1.78	12.42	1343.58
	OVC	JO-2	0.3	0.1	8.13	2.21	40	10	60	0.6	13	59.9	46.6	69.5	9.75	40.6	8.26	1.73	8.06	1.28	7.17	1.4	4.09	0.542	3.38	0.514	28.58	262.78	174.71	78.28	3.55	1.93	9.32	400.91
EST	RC	EST-1	0.24	0.3	10.8	2.04	90	20	130	0.6	26	90.4	86.4	87.9	15	59.3	12	2.71	12.3	1.9	10.3	2.03	5.73	0.791	4.82	0.733	23.66	392.31	260.60	116.70	4.53	2.07	12.11	706.66
		EST-2	0.26	0.2	12.6	1.78	50	10	60	0.7	26	38.4	60.8	65	7.99	29.2	5.27	1.14	5.01	0.82	5.04	0.99	2.99	0.458	3.12	0.501	26.07	226.73	168.26	52.32	7.26	1.30	13.17	414.12
		EST-3	0.29	0.5	19.8	2.96	50	20	80	1.1	36	62.8	72.7	94.2	11.6	43.2	7.5	1.61	7.43	1.29	8.11	1.62	4.97	0.717	4.86	0.801	17.56	323.41	229.20	85.17	6.10	1.24	10.11	635.54
	OVC	EST-4	0.31	0.2	9.75	2.12	40	20	60	0.7	14	52.1	52.5	80.2	11.2	43.5	8.46	1.79	7.81	1.24	7.17	1.39	3.84	0.525	3.58	0.555	25.43	223.76	195.86	70.40	3.91	1.77	9.91	436.21
		EST-5	0.44	0.1	12.7	2.63	20	50	50	0.9	11	32.1	41.3	74.7	9.15	33.9	6.4	1.18	5.63	0.92	5.38	1.02	3.18	0.468	2.99	0.479	21.19	186.70	165.45	46.54	4.06	1.53	9.33	327.82
Macropisoids			0.12	0.8	5.96	2.65	80	50	110	<0.5	25	85.2	88.1	120	17.7	73.7	15.1	3.27	15	2.07	10.8	2	5.82	0.759	4.48	0.693	27.23	444.69	314.60	111.82	3.67	2.71	13.29	846.98
			0.06	0.3	5.1	3.06	90	40	100	<0.5	20	94.1	77.8	87.4	13.6	55.9	11.2	2.62	12.3	1.78	9.83	1.94	5.23	0.669	4.05	0.608	26.93	379.03	245.90	118.21	4.37	2.46	12.98	719.53
			<0.05	0.2	4.89	1.86	50	20	60	<0.5	15	77.8	54.6	48	9.25	38.6	8.5	1.9	9.68	1.41	7.95	1.55	4.13	0.546	3.32	0.537	34.89	267.77	158.95	97.24	4.04	2.36	11.11	447.47
			<0.05	0.2	4.98	17.8	50	20	50	<0.5	16	73.8	48.1	74.7	9.97	42	9.05	2.36	10.8	1.63	8.66	1.67	4.41	0.56	3.5	0.56	9.15	291.77	183.82	94.79	3.35	2.50	9.29	605.57
			0.05	0.8	7.46	4.75	130	60	180	0.5	27	100	59.8	77.7	12	51.2	11.1	2.64	13.7	2.11	12.1	2.4	6.54	0.917	5.65	0.877	20.45	358.73	211.80	130.59	3.39	1.97	7.15	926.30

Fig. 2. a) Average content of major elements normalized to the UCC, b) Fe₂O₃-SiO₂-Al₂O₃ diagram of bauxite chemical classification (Aleva, 1994). RC = red clays, OVC = ochre and violet clays/marls. (For interpretation of the references to colour in this figure legend, the reader is referred to the web version of this article.)

4.2. Geochemical and transmission electron microscopy study of the critical metals

The RC and the macropisoids present higher average concentrations of critical metals (752.49 and 709.17 ppm, respectively) than the OVC (337.49 ppm) (Table 1).

Fig. 4 shows the concentrations of critical metals, according to the European Commission (2023), normalized to the UCC. Yttrium presents a high positive correlation with the HREEs ($r = 0.97$), which may indicate a similar behaviour that can be related with the fact that yttrium has similar ionic radius to that of the heavier REEs (e.g., holmium). For this reason, yttrium was considered along with the HREEs. The RC are enriched in all the critical metals, this enrichment being clearly higher in Sb (Fig. 4a). By contrast, the OVC are enriched in Sb, Hf, W and REEs, but depleted in the rest of the critical metals. Similarly, the macropisoids are enriched in certain metals (Sc, V, Co, In, Sb, W and REEs) and depleted in Ga, Ge, Nb, Hf, and Ta.

Both the RC and the macropisoids present higher average concentrations of LREEs (RC: 301.81 ppm and macropisoids: 223.01 ppm) than

HREEs (RC: 129.04 ppm and macropisoids: 110.53 ppm) than the OVC do (LREE: 161.23 ppm and HREE: 60.51 ppm). Chondrite-normalized REE patterns show that in the four stratigraphic profiles (Fig. 5a-d) and in the macropisoids (Fig. 5e), the LREE fractionation is higher than the HREE fractionation. By contrast, the HREEs in the ALC and EST profiles (Fig. 5a-b) show an almost horizontal slope, whereas in the VE and JO profiles and the macropisoids a slightly decreasing trend is observed in some samples (Fig. 5c-d). The (La/Sm)c average values (RC: 4.90; OVC: 3.93; macropisoids: 3.76) and the (Gd/Yb)c average values (RC: 1.53; OVC: 1.71; pisoids: 2.40) show that the RC exhibit higher fractionation of the LREE than the OVC and the macropisoids, whereas the latter exhibit higher fractionation of HREE than the clays (Fig. 5f).

The correlation coefficients obtained from the correlation matrix are represented in Table 2. All the critical metals (except the LREEs) show a significant correlation with Al ($r = 0.49$–0.98), Fe ($r = 0.53$–0.94, excepting Hf: 0.27), Ti ($r = 0.53$–0.99), and Th ($r = 0.53$–0.97). Nb, Sb, Hf, Ta, and W also present a good correlation with Zr ($r = 0.52$–0.99). On the other hand, all the critical metals (except Co, Sb, Hf, and the REEs) show a significant but negative correlation with K ($r = (-0.54)$–
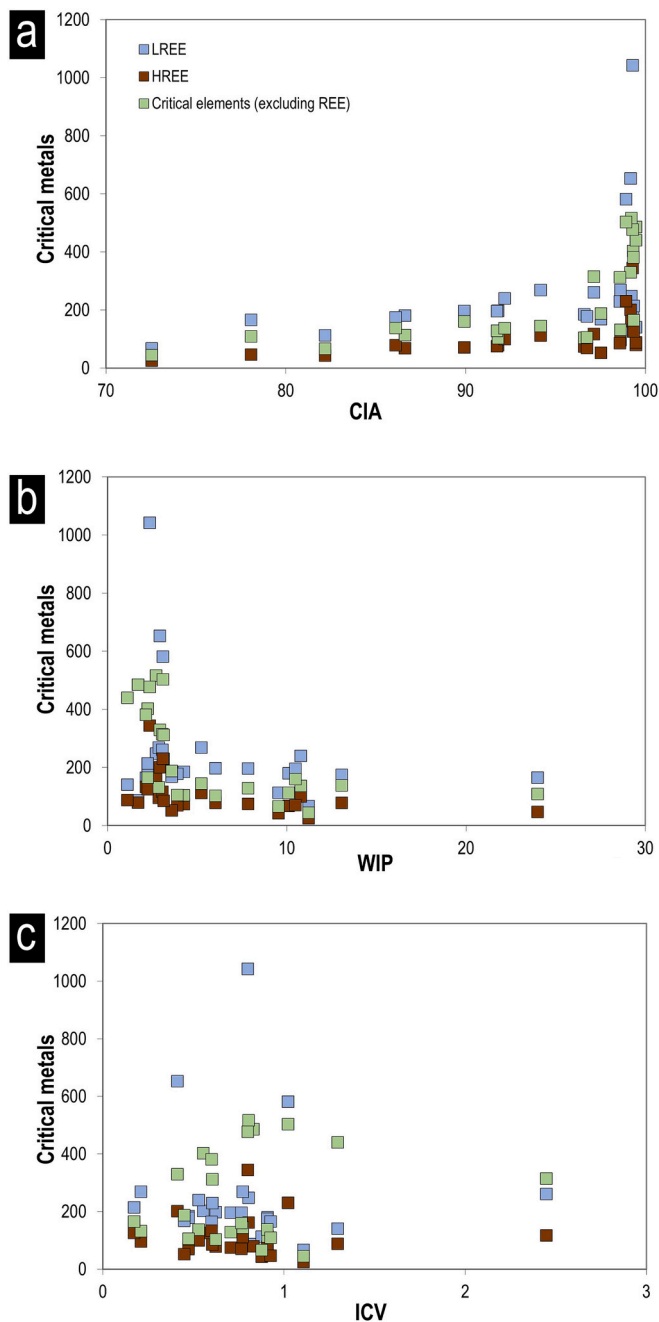
Fig. 3. Plot of CIA (a), WIP (b) and ICV (C) values from the red clays and ochre and violet clays/marls of the four profiles vs. their average critical metal content in parts per million (ppm). (For interpretation of the references to colour in this figure legend, the reader is referred to the web version of this article.)

(−0.62)).

When the five samples of macropisoids are included in the correlation matrix, V, Co, and Sb no longer show a significant correlation with Al (r = 0.10–0.34), but they do with P and Mn (r = 0.45–0.74). Both LREEs and HREEs show a significant correlation with Al (r = 0.45–0.55), Ti (r = 0.49–0.58), and Th (r = 0.50–0.59), but not with Fe (r = 0.17–0.33). Nb, Hf, Ta, and W still present a good correlation with Zr (r = 0.61–0.99), and some elements (Sc, V, Co, Ga, In, W) maintain a negative correlation with K ranging from r = −0.48 to r = −0.56.

The correlation coefficients between the critical metals and the mineral phases present in the samples (Table 2) show that all the elements (except Hf and the LREEs) have a significant positive correlation with kaolinite (r = 0.49–0.88) and a significant negative correlation

with the illitic phases from r = −0.48 to r = −0.70. Some elements also show significant correlation with other minerals: Sc, Ga, Nb, In, Ta, and W with diaspore (r = 0.48–0.61); Sc, V, Co, Ga, Ge, In, Sb, and W with hematite+goethite (r = 0.49–0.84); Sc, Nb, and Ta with anatase+rutile (r = 0.49–0.56); and Sc, V, Co, Nb, In, LREEs, and the HREEs with ilmenite (r = 0.50–0.66).

Again, when the macropisoids are included in the correlation matrix, some changes are detected. V, Co, and Sb no longer show a good correlation with kaolinite (r = 0.13–0.37). More elements (Sc, Ga, Ge, Nb, Hf, Ta, and W) present a significant correlation with diaspore (r = 0.48–0.69). The same elements (except for W) also have a significant correlation with anatase+rutile (r = 0.45–0.67). By contrast, hematite+goethite shows a correlation with V, Co, In, and Sb (r = 0.47–0.81), as does ilmenite with V (r = 0.44) and the LREEs (r = 45).

STEM images show the presence of single nanoparticles and/or aggregates of nanoparticles up to 100 nm in size. The detected elements are not hosted by the clay structures, but form discrete phases adsorbed on the surface of pseudohexagonal kaolinite crystals (Fig. 6).

These phases are smaller in size than the electron beam of the microscope, implying that the EDS analyses came from mixtures of these phases. The absence of stoichiometry in the chemical data of these particles (Table 3) may be due not only to the fact that the spot size of the TEM is higher than the REE-phases analysed, but also to the existence of solid solutions between them (Hay et al., 2013).

The EDS analyses make it possible to identify LREEs and HREEs (such as La, Ce and Nd and Y) that are forming phases with compositions close to monazite ($CePO_4$) and xenotime (YPO_4). The LREEs are also forming La, Ce and Nd oxides (Table 3). The STEM study also allowed zircon to be identified (enriched in yttrium).

The monazite-type phosphates present La (6.64) and Ce (8.41–25.5%) contents that are close to those of the theoretical monazite (La = 14.46%, Ce = 29.17%, Nd = 12.01%), although they do not contain Nd. By contrast, the xenotime-type phosphates present lower contents in Y (3.01–18.25) than the theoretical xenotime (Y = 48.35%). The analysed REE-oxides show compositions between lanthanum oxide (La_2O_3), cerium oxide (cerianite, CeO_2), and neodymium oxide (Nd_2O_3).

5. Discussion

5.1. Major elements and weathering processes

In the ALC and EST profiles, samples with higher Si content also present higher proportions of quartz and correspond to the OVC. The higher Si content of the RC in the VE profile is related to the fact that some lateritic levels located in the middle parts of this profile also contain quartz. By contrast, the Si content in the RC from the JO profile (sample JO-1) may proceed from kaolinite, since this sample contains almost no quartz (see the Supplementary Materials). Whatever the case, the Si concentrations normalized to the UCC showed an enrichment in the OVC and a depletion in the RC (Fig. 2a), indicating that in general there is an increase in the Si content towards the top of the profiles.

UCC-normalized data showed that the RC are enriched in Al and that the highest Al contents are in those RC levels with higher kaolinite and diaspore contents. In the same way, the higher Fe content in the RC is related to the higher goethite and hematite content of these samples and the higher Ti content in the RC also reflects the higher content of Ti oxides (rutile, anatase, and ilmenite) compared to the OVC (see Table 1 and Table S1). This difference in TiO_2 was not reported previously by Laita et al. (2020) since the contents in these phases were below the detection limit of XRD. Likewise, the enrichment in Mn probably reflects the presence of Mn-rich minerals that were not previously detected by XRD, especially in the macropisoids, where the Mn content is higher. Mn-oxyhydroxides and oxides such as asbolane, lithiophorite, and hollandite have previously been described in other laterites from Australia and Venezuela (e.g., Lottermoser, 1990; Domènech et al., 2022). According to Tupaz et al. (2021), these Mn-oxyhydroxides are difficult to
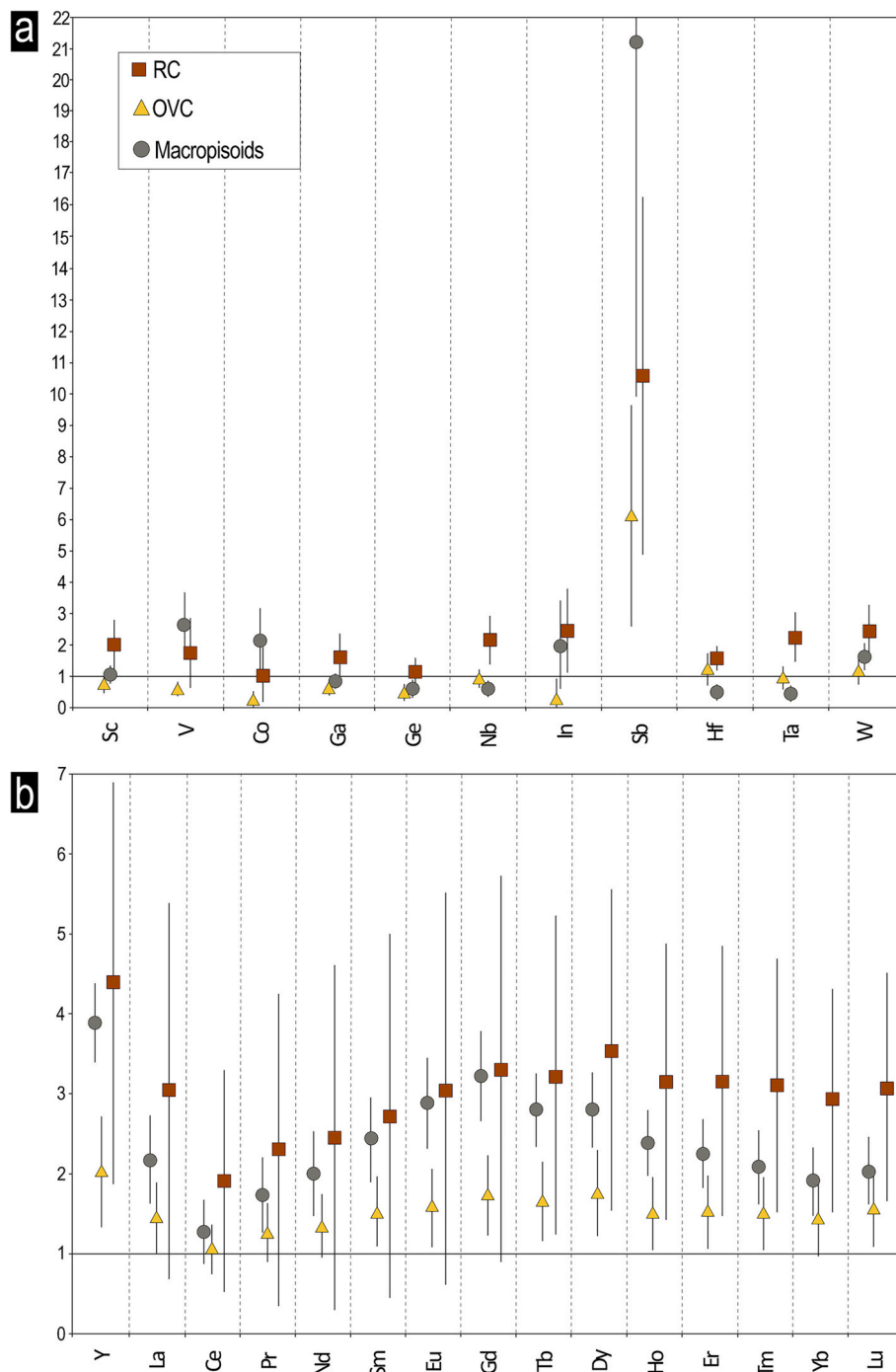
Fig. 4. a) Average critical metal (from Sc to W, excluding REEs) values normalized to the UCC, b) average REE values normalized to the UCC. RC = red clays, OVC = ochre and violet clays/marls. (For interpretation of the references to colour in this figure legend, the reader is referred to the web version of this article.)

identify by conventional X-ray powder diffraction since they are fine-grained and poorly crystalline in nature. The higher K and Mg content of the OVC is related to the presence of illitic phases and beidellite in these samples, whereas the higher Fe content of the macropisoids reflects a higher presence of hematite and goethite.

The Si content of the samples comes from quartz and the clay minerals. According to Laita et al. (2020), the quartz and illite present in the lateritic palaeosols are of detrital origin, so the occurrence of these minerals could increase the Si content of the palaeosols. The presence of Si proceeding from detrital quartz and illite, whose contents are higher in the ochre and violet clays/marls, may have caused these samples to be classified as kaolinites, when they most probably correspond to laterites

or ferritic kaolinites (Fig. 2b).

In general, CIA values from 50 to 75 indicate muscovite, illite, smectite, and feldspar compositions, reflecting moderate weathering conditions, whereas CIA values close to 100 reveal more intense weathering, resulting in the genesis of kaolinite (Fedo et al., 1995; Bauluz et al., 2000; Bahlburg and Dobrzinski, 2015). By contrast, the optimum weathered valued for the WIP index is 0 (Price and Velbel, 2003). In our samples, the RC showed an average CIA value of 98 and average WIP value of 3, which are closer to 100 and 0, respectively, comparing with the average CIA and WIP values obtained for the OVC (CIA = 85 and WIP = 12). The absence of a clear tendency in the ICV values reflects that there is no relation between the abundance of
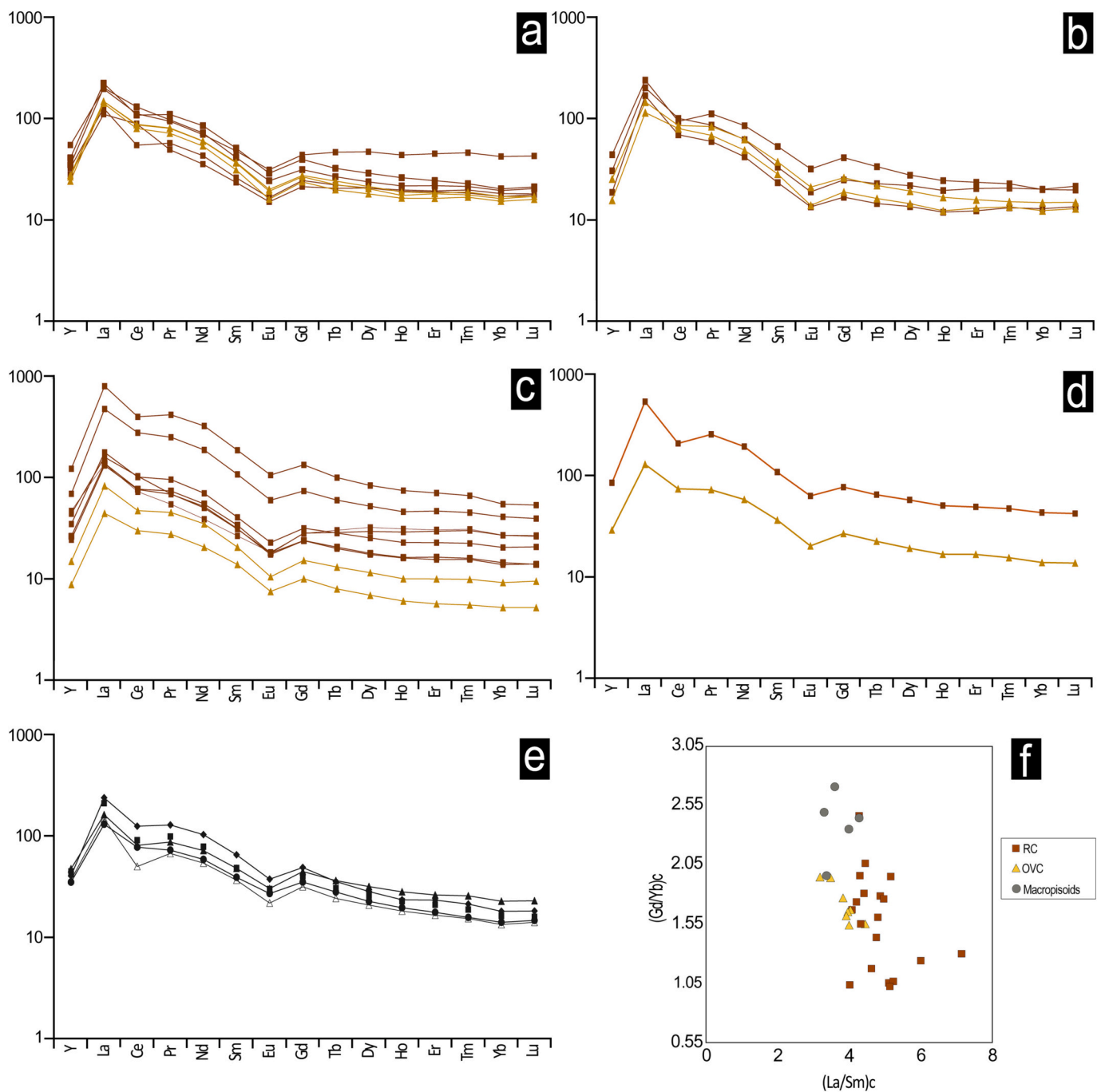
Fig. 5. Chondrite-normalized REE + Y patterns of the lateritic samples in the ALC (a), EST (b), VE (c) and JO (d) profiles and of the macropisoids (e). Plot of the average (La/Sm)c vs. (Gd/Yb)c values in the red clays and the ochre and violet clays/marls of all the profiles, and the macropisoids (f). RC = red clays, OVC = ochre and violet clays/marls. (For interpretation of the references to colour in this figure legend, the reader is referred to the web version of this article.)

alumina and other major elements in the lateritic palaeosols.

The CIA values of the four profiles decrease towards the top, and this decrease is most pronounced in the VE profile (see Table S3 in the Supplementary Materials), which coincides with a higher content of illite in the OVC of this profile, reflecting a greater detrital influence related to a lower degree of weathering. In this case, the Si from the detrital phases has not prevented a decrease in CIA values being observed towards the top of the profiles, corroborating the decrease in the intensity of chemical weathering described by Laita et al. (2020).

5.2. Concentration and distribution of critical metals

5.2.1. Critical metals and weathering intensity

The higher the CIA value and the lower WIP value, the higher the content of critical metals in the lateritic palaeosols (Fig. 3a and b), indicating that the concentration of critical metals increases with weathering. However, a previous study on nearby Lower Cretaceous karst bauxites (Yuste et al., 2017) reported a loss of all REE + Y during the transformation of clays into pisolitic bauxites, reflecting the fact that very intense chemical weathering processes (i.e., bauxitization) could trigger a depletion in REEs.

In this study, the fractionation of the LREEs was higher in the RC

Table 2

Correlation coefficients (r) from the correlation matrix obtained from the mineralogical and geochemical data of the lateritic samples (n = 25) and of the lateritic samples+macropisoids (n = 30). The correlation coefficients show a significance level of 0.01 for r = 0.49 and r = 0.45, and 0.001 for r = 0.60 and r = 0.55 for the lateritic samples (RC + OVR) and the lateritic samples+macropisoids, respectively. Kaol = kaolinite, I = illite, Sm = smectite (beidellite-type), Dsp = diaspore, Hem = hematite, Gt = goethite, Ant = anatase, Rt = rutile, Ilm = ilmenite.

		Al$_2$O$_3$	Fe$_2$O$_3$	MnO	P$_2$O$_5$	K$_2$O	TiO$_2$	Zr	Th
Laterites	Sc	0.92	0.81	0.03	0.21	−0.6	0.91	0.48	0.93
	V	0.7	0.94	0.16	0.19	−0.54	0.67	0.31	0.78
	Co	0.56	0.81	0.58	0.37	−0.43	0.53	0.11	0.53
	Ga	0.93	0.77	−0.03	0.08	−0.62	0.9	0.46	0.94
	Ge	0.88	0.76	−0.07	0.06	−0.54	0.9	0.55	0.95
	Nb	0.98	0.56	−0.21	0.09	−0.58	0.99	0.59	0.96
	In	0.86	0.75	0.04	0.15	−0.61	0.81	0.32	0.83
	Sb	0.64	0.77	−0.08	−0.09	−0.4	0.65	0.52	0.79
	Zr	0.49	0.22	−0.31	−0.31	−0.23	0.62	1	0.64
	Hf	0.59	0.27	−0.33	−0.28	−0.28	0.77	0.99	0.73
	Ta	0.97	0.53	−0.26	−0.03	−0.59	0.99	0.65	0.97
	W	0.92	0.64	−0.2	−0.07	−0.59	0.95	0.66	0.97
	∑REE	0.53	0.44	0.08	0.15	−0.33	0.57	0.44	0.58
	∑LREE	0.47	0.41	0.07	0.15	−0.3	0.53	0.42	0.54
	∑HREE	0.64	0.57	0.1	0.15	−0.43	0.69	0.51	0.71
Laterites + macropisoids	Sc	0.9	0.26	−0.17	−0.11	−0.49	0.88	0.53	0.9
	V	0.34	0.82	0.51	0.45	−0.56	0.28	−0.02	0.36
	Co	0.14	0.78	0.74	0.56	−0.48	0.09	−0.21	0.09
	Ga	0.91	0.24	−0.19	−0.14	−0.5	0.88	0.52	0.9
	Ge	0.87	0.21	−0.21	−0.17	−0.41	0.87	0.6	0.91
	Nb	0.98	−0.07	−0.48	−0.31	−0.35	0.99	0.71	0.97
	In	0.69	0.54	0.17	0.22	−0.56	0.63	0.22	0.64
	Sb	0.1	0.78	0.63	0.5	−0.42	0.07	−0.05	0.14
	Zr	0.63	−0.33	−0.59	0.52	−0.01	0.74	1	0.76
	Hf	0.7	−0.31	−0.61	−0.52	−0.04	0.8	0.99	0.81
	Ta	0.98	−0.11	−0.52	−0.36	−0.33	0.99	0.76	0.98
	W	0.87	0.29	−0.17	−0.08	−0.49	0.88	0.61	0.89
	∑REE	0.49	0.2	0.02	0.01	−0.3	0.51	0.38	0.52
	∑LREE	0.45	0.17	−0.01	−0.01	−0.27	0.49	0.37	0.5
	∑HREE	0.55	0.33	0.1	0.08	−0.42	0.58	0.4	0.59

		Kaol	I	Sm	Dsp	Hem + Gt	Ant + Rt	Ilm
Laterites	Sc	0.82	−0.66	−0.28	0.48	0.67	0.5	0.66
	V	0.63	−0.53	−0.27	0.2	0.84	0.32	0.55
	Co	0.49	−0.5	−0.18	0.15	0.82	0.27	0.5
	Ga	0.82	−0.65	−0.29	0.48	0.68	0.43	0.48
	Ge	0.79	−0.7	−0.26	0.42	0.62	0.46	0.47
	Nb	0.88	−0.68	−0.28	0.6	0.43	0.56	0.5
	In	0.74	−0.57	−0.21	0.55	0.66	0.45	0.54
	Sb	0.52	−0.44	−0.31	0.20	0.60	0.21	0.34
	Hf	0.46	−0.64	−0.19	0.41	0.08	0.18	0.3
	Ta	0.87	−0.69	−0.31	0.61	0.4	0.49	0.42
	W	0.82	−0.65	−0.35	0.52	0.49	0.4	0.39
	∑REE	0.4	−0.4	−0.18	0.32	0.37	0.25	0.56
	∑LREE	0.35	−0.36	−0.14	0.29	0.32	0.24	0.57
	∑HREE	0.53	−0.48	−0.27	0.37	0.47	0.26	0.51
Laterites + macropisoids	Sc	0.79	−0.56	−0.22	0.52	0.14	0.54	0.43
	V	0.37	−0.53	−0.29	−0.03	0.77	0.02	0.44
	Co	0.21	−0.49	−0.22	−0.12	0.81	−0.09	0.37
	Ga	0.78	−0.54	−0.23	0.53	0.15	0.49	0.29
	Ge	0.74	−0.57	−0.20	0.48	0.1	0.52	0.27
	Nb	0.8	−0.46	−0.16	0.68	−0.18	0.67	0.23
	In	0.57	−0.53	−0.21	0.43	0.47	0.32	0.41
	Sb	0.13	−0.41	−0.28	−0.14	0.76	−0.19	0.27
	Hf	0.44	−0.33	−0.05	0.55	−0.43	0.45	0.04
	Ta	0.78	−0.44	−0.18	0.69	−0.22	0.63	0.17
	W	0.74	−0.57	−0.31	0.52	0.16	0.42	0.33
	∑REE	0.39	−0.38	−0.17	0.3	0.15	0.24	0.44
	∑LREE	0.35	−0.33	−0.12	0.29	0.1	0.24	0.45
	∑HREE	0.48	−0.48	−0.27	0.32	0.29	0.2	0.39

(lower, more weathered levels) than in the OVC (middle-upper, less weathered levels), which would support the hypothesis that the more intense the chemical weathering, the more LREE depletion can be expected (Maksimovic and Pantó, 1991). This higher LREE than HREE fractionation also indicates that the HREEs were less mobile than the LREEs during weathering as occur in nearby karst bauxites (Yuste et al., 2017; Yuste et al., 2020). Nevertheless, the LREE content in the RC is higher than in the OVC. Together with the presence of LREE phosphates

and oxides in the RC (as evidenced by STEM images and EDS analyses), this demonstrates that the laterization did not give rise to such an intense chemical weathering process as would occur during bauxitization.

5.2.2. Forms and distribution of critical metals in the lateritic palaeosols

REE enrichment in weathered rocks can be linked to the accumulation of detrital minerals such as detrital monazite and xenotime, as has
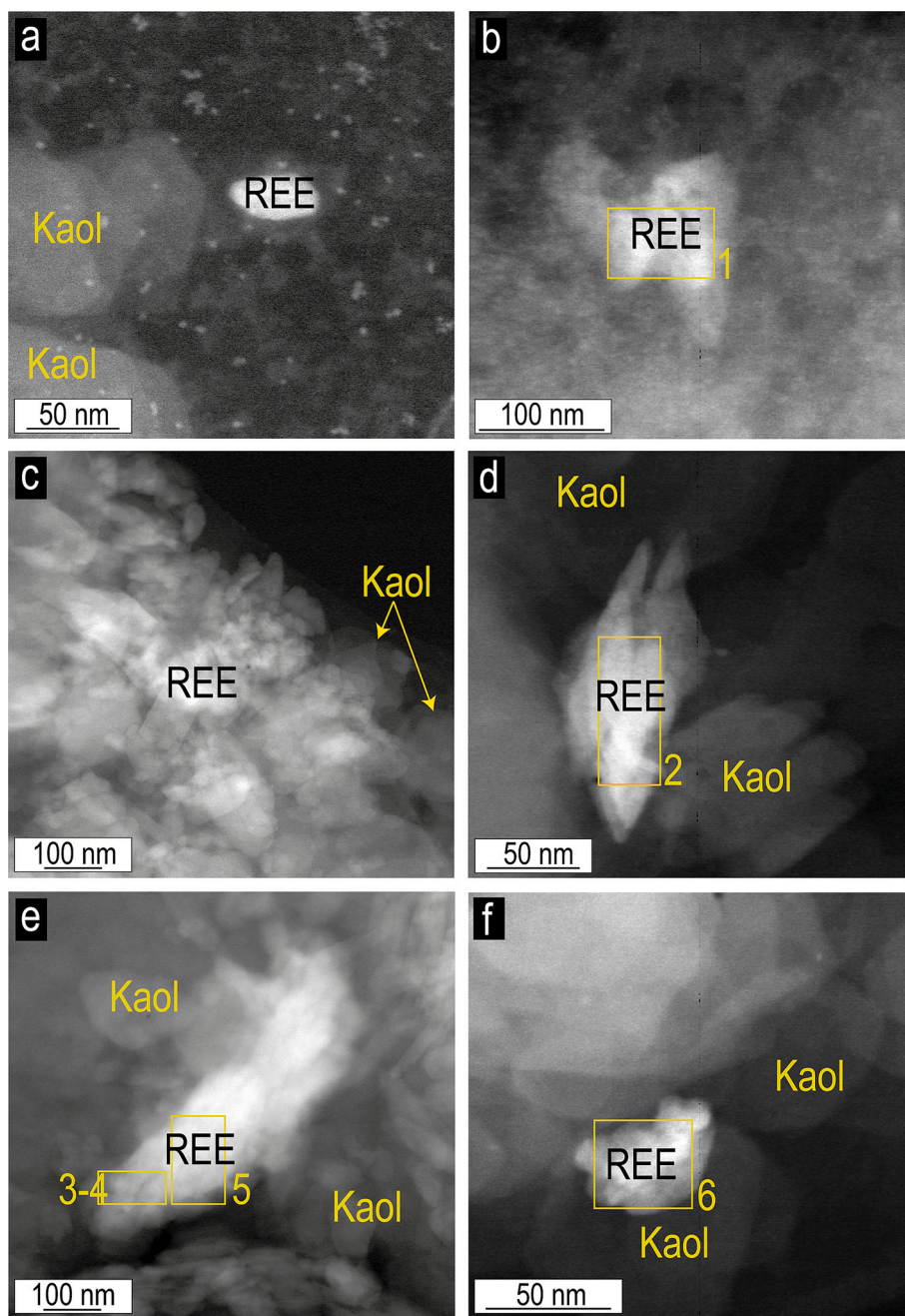
Fig. 6. STEM images showing critical metal phases adsorbed on the surface of pseudohexagonal kaolinite crystals in the red clays of the ALC (a and b), JO (c), and VE (d-f) profiles. Kaol = kaolinite, REE = REE-phases. (For interpretation of the references to colour in this figure legend, the reader is referred to the web version of this article.)

been described in other bauxites from China, Italy, and Spain (e.g., Putzolu et al., 2018; Reinhardt et al., 2018; Luo et al., 2023), but REE fractionation can also take place through the formation of authigenic REE-bearing minerals (Maksimovic and Pantó, 1991; Horbe and Costa, 1999; Yuste et al., 2020). Furthermore, REEs can also fractionate during laterization (Braun et al., 1998; Al-Khirbash et al., 2014; Guimapi et al., 2023) and be adsorbed on the surface of Fe-rich phases or clay minerals (Wang et al., 2010; Mameli et al., 2007).

All the critical metals in the lateritic palaeosols and macropisoids are related to Al, indicating that these elements can be adsorbed on the clay minerals. The adsorption capacity of the clay minerals is determined by their composition, specific surface, and charge surface (Yusoff et al., 2013). Under natural pH conditions, those clay minerals with a negative layer charge can adsorb REEs effectively through various processes: ion

exchange, surface complexation, electrostatic attraction, and migration into clay structure (Yang, M. et al., 2019). Accordingly, 2:1 clay minerals (e.g., smectite or illite) have higher adsorption capacities than the 1:1 kaolin-group.

On the other hand, the point of zero charge (PZC) (i.e., the pH at which the net total particle charge is zero) also plays an important role in the variable-charge surfaces of soils. When the pH is greater than the PZC, exchange of cations can occur, whereas anions will be retained if the pH value is less than the PZC (Appel et al., 2003). Some authors (Appel et al., 2003; Yang, M et al., 2019) have reported PZC values for kaolinite (PZC = 3.8–4.1), illite (PZC = ~2.5), and smectite (PZC = 7–9). According to these values, for a pH range of 4–7, kaolinite, illite and smectite can adsorb REEs, but Kaolinite has a higher sorption affinity to REEs due to more favourable electrostatic effects for adsorption

Table 3
EDS analysis (Wt%) of the areas analysed by STEM of nanoparticle phases corresponding to the images from Fig. 6. Uncertainty of the analyses in brackets.

	Mineral phase	O	P	Ca	Y	Zr	La	Ce	Nd
1	Monazite-type phosphate	76.46 (1.93)	9.77 (0.45)	–	–	–	–	13.75 (0.63)	–
2	Zircon-Xenotime?	67.00 (1.41)	8.34 (1.01)	0.53 (0.14)	18.25 (0.99)	5.86 (0.66)	–	–	–
3	REE-oxide	84.92 (3.17)	1.43 (0.41)	–	–	–	4.00 (1.68)	–	9.64 (1.76)
4	Monazite-type phosphate	65.42 (3.87)	4.42 (0.51)		–	–	6.64 (2.05)	25.5 (2.08)	
5	REE-oxide	45.48 (1.17)	0.8 (0.14)	2.39 (0.17)	3.03 (0.39)	–	27.70 (0.72)	20.58 (0.83)	–
6	Xenotime-type phosphate	55.49 (3.15)	12.16 (1.08)	7.84 (0.52)	3.01 (2.05)		13.05 (1.74)	8.41 (1.89)	

due to the low PZC compared to smectite (Coppin et al., 2002; Stumpf et al., 2002). Together with the low proportions of smectite present in the lateritic palaeosols (<5 to 17%) (see Table S1 in the Supplementary Materials), this could explain the absence of correlation between the critical metals and smectite in the lateritic palaeosols (Table 2). The higher positive correlation of the critical metals with the authigenic kaolinite and the negative correlation with the detrital illite (Table 2), suggest that, in this case, authigenic kaolinite was the clay mineral that adsorbed the critical metals during the laterization process. STEM images (Fig. 6) corroborate that some elements, such as Y, La, Ce and Nd, form discrete phases that are adsorbed on the surface of authigenic kaolinite crystals. The REE fractionation that took place during weathering would have given rise to the genesis of the analysed LREE-phases. In addition, the presence of Y in the RC reflects the fact that although HREEs are less mobile during chemical weathering, xenotime-type phosphates can also be formed.

In addition, many of the critical metals in the lateritic palaeosols are correlated, not only with Al but also with the Fe and Ti-oxides. According to Kühnel (1987), hematite is a major scavenger of cations from solutions and goethite also exert an important scavenging action relative to aqueous ions. This is because metal oxides have a strong tendency for specific ion adsorption, as has been demonstrated in experimental models (e.g., Rabung et al., 1998; Rabung et al., 2000; Vermeer et al., 1999) and described in soil systems (e.g., McLaren et al., 1986; Bradl, 2004). In Mediterranean bauxites, it has been described that the Fe-rich horizons concentrate Co, Ni, Cr, V and REE and that authigenic heavy minerals like rutile, anatase and titanite are scavenging HREE (Mongelli, 1997; Mameli et al., 2007; Yuste et al., 2017). Hematite and anatase phases scavenging REE have also been described in bauxites from China (Luo et al., 2023). The positive correlation of the HREEs with hematite, goethite, anatase, rutile and ilmenite observed in the studied lateritic palaeosols (Table 2) may be, therefore, indicating that these minerals acted as scavengers for less mobile HREEs. In the same way, the significant positive correlation of LREEs with Ti and ilmenite could indicate that Ti and Fe-bearing minerals may act as scavengers for the LREEs.

The good positive correlation of Nb, Sb, Hf, Ta, and W with Zr may reflect the presence of zircons enriched in these metals, or alternatively phases of similar size to zircon. Zircon accumulation can lead to slight enrichments in Th (Bauluz et al., 2000), and the good positive correlation of all the analysed critical metals with Th could also indicate the presence of some Th-phase (e.g., thorite), as has been described in other laterites from Brazil (Horbe and Costa, 1999). The EDS analyses show intermediate compositions between xenotime and zircon, which could correspond to a solid solution of the thorite–xenotime–zircon–coffinite system (Förster, 2006). By contrast, this good correlation between zircon and the critical metals may also result from zircon crystals surrounding xenotime crystals, as has been described in bauxites from China (Luo et al., 2023).

When the macropisoids were considered in the correlation matrix (Table 2), Co, V, and Sb showed a better correlation with Fe, P, and Mn. Fe oxides can control Co and V distribution due to the higher sensitivity

to redox conditions of these elements (Abedini et al., 2022; Yuste et al., 2017), and so the hematite and goethite included in the macropisoids could control their distribution. Authigenic REE-phosphates (e.g., xenotime) have been described in bauxitic deposits (Luo et al., 2023). Given the good correlation with P, phosphates containing Co, V, or Sb may also be included in the macropisoids, although in low proportions, since they were not previously identified by XRD or FESEM.

6. Conclusions

The following conclusions are drawn from these geochemical and STEM studies of Lower Cretaceous lateritic palaeosols from NE Iberia:

1) The major element concentrations reflect the mineralogical composition of the samples. The red clays from the lower levels of the profiles are more enriched in Al, Fe, and Ti due to their higher content in kaolinite, diaspore, hematite, goethite, rutile, anatase, and ilmenite. The ochre and violet clays/marls from the middle and upper levels of the profiles are enriched in Si and present higher quantities of K and Mg, reflecting their higher content in quartz, illitic phases, and smectite. The macropisoids are mainly enriched in Fe and Mn and are somewhat enriched in P due to their higher content in hematite and goethite and the probable presence of Mn-oxyhydroxides and critical-metal-rich phosphates.
2) The higher LREE than HREE fractionation in the laterites indicates that the HREEs were less mobile than the LREEs during chemical weathering. The positive correlation of the HREEs with hematite, goethite, anatase, and rutile and the positive correlation of the LREEs with ilmenite show that these Fe- and Ti-minerals acted as scavengers for some of the REEs.
3) The good correlation of all the critical metals (including the REEs) not only with Ti and Fe, but also with Al, indicates that they can also be adsorbed on clay minerals. The better correlation of these elements with authigenic kaolinite and the negative correlation with detrital illitic phases suggest that kaolinite is the clay mineral that controls their distribution. This is corroborated by the STEM images and the EDS analyses that show xenotime, monazite, and La, Ce and Nd oxides adsorbed on the surface of kaolinites.
4) The decrease in the CIA and the increase in the WIP values from the red clays to the ochre and violet clays/marls reflect a decrease in the intensity of chemical weathering towards the top of the profiles. Although intense chemical weathering processes could have prevented the concentration of certain elements (e.g., LREEs), the decrease in the critical metal content coincides with the decrease in the CIA values and the increase in the WIP values, reflecting the fact that, in this case, the concentration of the critical metals increased during laterization.

CRediT authorship contribution statement

Elisa Laita: Writing – review & editing, Writing – original draft,

Methodology, Investigation, Formal analysis, Data curation, Conceptualization. **Blanca Bauluz:** Writing – review & editing, Writing – original draft, Supervision, Resources, Project administration, Investigation, Funding acquisition, Conceptualization. **Alfonso Yuste:** Writing – review & editing, Writing – original draft, Supervision, Methodology, Investigation, Formal analysis, Data curation.

Declaration of competing interest

The authors declare that they have no known competing financial interests or personal relationships that could have appeared to influence the work reported in this paper.

Data availability

Data will be made available on request.

Acknowledgements

Appendix A. Supplementary data

Supplementary data to this article can be found online at https://doi.org/10.1016/j.clay.2024.107264.

References

Abedini, A., Mongelli, G., Khosravi, M., 2022. Geochemistry of the early Jurassic Soleiman Kandi karst bauxite deposit, Irano–Himalayanbelt, NW Iran: Constraints on bauxite genesis and the distribution of critical raw materials. J. Geochem. Explor. 241, 107056 https://doi.org/10.1016/j.gexplo.2022.107056.

Aleva, G.J.J., 1994. Laterites: Concepts, Geology, Morphology and Chemistry. International Soil Reference and Information Centre (ISRIC), Wageningen, The Netherlands.

Al-Khirbash, S., Semhi, K., Richard, L., Nasir, S., Al-Harthy, A., 2014. Rare earth element mobility during laterization of mafic rocks of the Oman ophiolite. Arab. J. Geosci. 7, 5443–5454. https://doi.org/10.1007/s12517-013-1189-6.

Appel, C., Ma, L.Q., Dean Rhue, R., Kennelley, E., 2003. Point of zero charge determination in soils and minerals via traditional methods and detection of electroacoustic mobility. Geoderma 113, 77–93. https://doi.org/10.1016/S0016-7061(02)00316-6.

Bahlburg, H., Dobrzinski, N., 2015. A review of the Chemical Index of Alteration (CIA) and its application to the study of Neoproterozoic glacial deposits and climate transitions. In: Arnaud, E., Halverson, G.P., Shields-Zhou, G. (Eds.), The Geological Record of Neoproterozoic Glaciations, vol. 36. Geological Society, London, Memoirs, pp. 81–92. https://doi.org/10.1144/M36.6.

Bauluz, B., Mayayo, M.J., Fernandez-Nieto, C., Gonzalez Lopez, J.M., 2000. Geochemistry of Precambrian and Paleozoic siliciclastic rocks from the Iberian Range NE Spain: implications for source-area weathering, sorting, provenance, and tectonic setting. Chem. Geol. 168, 135–150. https://doi.org/10.1016/S0009-2541(00)00192-3.

Bradl, B., 2004. Adsorption of heavy metal ions on soils and soils constituents. J. Colloid Interface Sci. 277 (1), 1–18. https://doi.org/10.1016/j.jcis.2004.04.005.

Braun, J.J., Viers, J., Dupré, B., Polve, M., Ndam, J., Muller, J.P., 1998. Solid/liquid REE fractionation in the lateritic system of Goyoum, East Cameroon: the implication for the present dynamics of the soil covers of the humid tropical regions. Geochim. Cosmochim. Acta 62 (2), 273–299. https://doi.org/10.1016/S0016-7037(97)00344-X.

Chakhmouradian, A.R., Smith, M.P., Kynickly, J., 2015. From "strategic"-tungsten to "green"-neodymium: a century of critical metals at a glance. Ore Geol. Rev. 64, 455–458. https://doi.org/10.1016/j.oregeorev.2014.06.008.

Coppin, F., Berger, G., Bauer, A., Castet, S., Loubet, M., 2002. Sorption of lanthanides on smectite and kaolinite. Chem. Geol. 182, 57–68. https://doi.org/10.1016/S0009-2541(01)00283-2.

Cox, R., Lowe, D.R., Cullers, R.L., 1995. The influence of sediment recycling and basement composition on evolution of mudrock chemistry in the southwestern United States. Geochim. Cosmochim. Acta 59 (14), 2919–2940. https://doi.org/10.1016/0016-7037(95)00185-9.

Domènech, C., Villanova-de-Benavent, C., Proenza, J.A., Tauler, E., Lara, L., Galí, S., Soler, J.M., Campeny, M., Ibañez-Insa, J., 2022. Co–Mn mineralisations in the Ni

laterite deposits of Loma Caribe (Dominican Republic) and Loma de Hierro (Venezuela). Minerals 12, 927. https://doi.org/10.3390/min12080927.

European Commission, 2023. Study on the Critical Raw Materials for the EU 2023-Final Report. Publications Office of the European Union, Luxembourg, p. 2023, 158 pp. https://doi.org/10.2873/725585.

Fedo, C.M., Nesbitt, H.W., Young, G.M., 1995. Unravelling the effects of potassium metasomatism in sedimentary rocks and paleosols, with implications for paleoweathering conditions and provenance. Geology 23, 921–924. https://doi.org/10.1130/0091-7613(1995)023<0921:UTEOPM>2.3.CO;2.

Förster, H.-J., 2006. Composition and origin of intermediate solid solutions in the system thorite–xenotime–zircon–coffinite. Lithos 88, 35–55. https://doi.org/10.1016/j.lithos.2005.08.003.

Guimapi, N.T., Tematio, P., Tiomo, I.F., Happi, F.D., Fotso, A.K., Tchaptchet, C.W.T., 2023. Redistribution and fractionation of trace and rare earth elements during weathering and lateritization of orthogneiss in Ndokayo (Bétaré-Oya Gold District, South East Cameroon). Geoderma Region. 32 https://doi.org/10.1016/j.geodrs.2022.e00601 e00601.

Gunn, G., 2014. Critical Metals Handbook. John Wiley & Sons, Ltd.

Hay, R.S., Mogilevsky, P., Boakye, E., 2013. Phase transformations in xenotime rare-earth orthophosphates. Acta Mater. 61, 6933–6947. https://doi.org/10.1016/j.actamat.2013.08.005.

Horbe, A.M.C., Costa, M.L.D., 1999. Geochemical evolution of a lateritic Sn Zr Th Nb Y REE-bearing ore body derived from apogranite: the case of Pitinga, Amazonas-Brazil. J. Geochem. Explor. 66, 339–351. https://doi.org/10.1016/S0375-6742(99)00002-3.

Kühnel, R.A., 1987. The role of cationic and anionic scavengers in laterites. Chem. Geol. 60 (1–4), 31–40. https://doi.org/10.1016/0009-2541(87)90107-0.

Laita, E., Bauluz, B., Aurell, M., Bádenas, B., Canudo, J.I., Yuste, A., 2020. A change from warm/humid to cold/dry climate conditions recorded in lower Barremian clay-dominated continental successions from the SE Iberian Chain (NE Spain). Sediment. Geol. 403, 105673 https://doi.org/10.1016/j.sedgeo.2020.105673.

Laita, E., Subirana, M.A., Schaumloffel, D., Yuste, A., Bauluz, B., 2023. NanoSIMS as an analytical tool for measuring oxygen and hydrogen isotopes in clay minerals from palaeosols: Analytical procedure and preliminary results. Chem. Geol. 615, 121213 https://doi.org/10.1016/j.chemgeo.2022.121213.

Linnen, R.L., Samson, I.M., Williams-Jones, A.E., Chakhmouradian, A.R., 2014. Geochemistry of the rare-earth elements, Nb, Ta, Hf and Zr deposits. In: Holland, H. D., Turekian, K. (Eds.), Treatise on Geochemistry, , 2nd ed.vol. 13. Elsevier, p. 650. https://doi.org/10.1016/B978-0-08-095975-7.01124-4.

Lottermoser, B.G., 1990. Rare-earth element mineralisation within the Mt. Weld carbonatite laterite, Western Australia. Lithos 24, 151–167. https://doi.org/10.1016/0024-4937(90)90022-S.

Luo, C., Liang, P., Yang, R., Gao, J., Chen, Q., Mo, H., 2023. Mineralogical and geochemical constraints on the occurrence forms of REEs in carboniferous karst bauxite, Central Guizhou Province, Southwest China: a case study of lindai bauxite. Minerals 13, 320. https://doi.org/10.3390/min13030320.

Maksimovic, Z., Pantó, G., 1991. Contribution to the geochemistry of the rare earthelements in the karst-bauxite deposits of Yugoslavia and Greece. Geoderma 51, 93–109. https://doi.org/10.1016/0016-7061(91)90067-4.

Mameli, P., Mongelli, G., Oggiano, G., Dinelli, E., 2007. Geological, geochemical and mineralogical features of some bauxite deposits from Nurra (Western Sardinia, Italy): insights on conditions of formation and parental affinity. Int. J. Earth Sci. (Geol. Rund.) 96, 887–902. https://doi.org/10.1007/s00531-006-0142-2.

McLaren, R.G., Lawson, D.M., Swift, R.S., 1986. Sorption and desorption of cobalt by soils and soil components. J. Soil Sci. 37 (3), 413–426. https://doi.org/10.1111/j.1365-2389.1986.tb00374.x.

Mongelli, G., 1997. Ce-anomalies in the textural components of Upper cretaceous karst bauxites from the Apulian carbonate platform (southern Italy). Chem. Geol. 140 (2), 69–79. https://doi.org/10.1016/S0009-2541(97)00042-9.

Mongelli, G., Boni, M., Oggiano, G., Mameli, P., Sinisi, R., Buccione, R., Mondillo, N., 2017. Critical metals distribution in Tethyan karst bauxite: the cretaceous Italian ores. Ore Geol. Rev. 86, 526–536. https://doi.org/10.1016/j.oregeorev.2017.03.017.

Mongelli, G., Mameli, P., Sinisi, R., Buccione, R., Oggiano, G., 2021. Rees and other critical raw materials in cretaceous Mediterranean-type bauxite: the case of the Sardinian ore (Italy). Ore Geol. Rev. 139 (Part B), 104559. https://doi.org/10.1016/j.oregeorev.2021.104559.

Nesbitt, H.W., Young, G.M., 1982. Early Proterozoic climates and plate motions inferred from major element chemistry of lutites. Nature 299, 715–717. https://doi.org/10.1038/299715a0.

Parker, A., 1970. An index of weathering for silicate rocks. Geol. Mag. 107, 501–504. https://doi.org/10.1017/S0016756800058581.

Price, J.R., Velbel, M.A., 2003. Chemical weathering indices applied to weathering profiles developed on heterogeneous felsic metamorphic parent rocks. Chem. Geol. 202 (3–4), 397–416. https://doi.org/10.1016/j.chemgeo.2002.11.001.

Putzolu, F., Papa, A.P., Mondillo, N., Boni, M., Balassone, G., Mormone, A., 2018. Geochemical characterization of bauxite deposits from the Abruzzi Mining District (Italy). Minerals 8, 298. https://doi.org/10.3390/min8070298.

Rabung, T., Geckeis, H., Kim, J.I., Beck, H.P., 1998. Sorption of Eu (III) on a natural hematite: application of a surface complexation model. J. Colloid Interface Sci. 208 (1), 153–161. https://doi.org/10.1006/jcis.1998.5788.

Rabung, T., Stumpf, T., Geckeis, H., Klenze, R., Kim, J.I., 2000. Sorption of Am (III) and Eu (III) onto γ-alumina: experiment and modelling. Radiochim. Acta 88 (9–11), 711–716. https://doi.org/10.1524/ract.2000.88.9-11.711.

Reinhardt, N., Proenza, J.A., Villanova-de-Benavent, C., Aiglsperger, T., Bover-Arnal, T., Torró, L., Salas, R., Dziggel, A., 2018. Geochemistry and mineralogy of rare earth

elements (REE) in bauxitic ores of the Catalan Coastal Range, NE Spain. Minerals 8, 562. https://doi.org/10.3390/min8120562.

Stumpf, T., Bauer, A., Coppin, F., Fanghänel, T., Kim, J.I., 2002. Inner-sphere, outer-sphere and ternary surface complexes: a TRLFS study of the sorption process of Eu (III) onto smectite and kaolinite. Radiochim. Acta 90 (6), 345–349. https://doi.org/10.1524/ract.2002.90.6.345.

Taylor, S.R., McLennan, S.M., 1985. The Continental Crust: Its Composition and Evolution. An Examination of the Geochemical Record Preserved in Sedimentary Rocks. Blackwell Scientific, Oxford, U.K, 113 p.

Tupaz, C.A., Watanabe, Y., Sanematsu, K., Echigo, T., 2021. Spectral and chemical studies of iron and manganese oxyhydroxides in laterite developed on ultramafic rocks. Resour. Geol. 71, 377–391. https://doi.org/10.1111/rge.12272.

Vermeer, A.W., McCulloch, J.K., Van Riemsdijk, W.H., Koopal, L.K., 1999. Metal ion adsorption to complexes of humic acid and metal oxides: deviations from the additivity rule. Environ. Sci. Technol. 33 (21), 3892–3897. https://doi.org/10.1021/es990260k.

Wang, Q.F., Deng, J., Liu, X.F., Zhang, Q.Z., Sun, S.L., Jiang, C.Z., Zhou, F., 2010. Discovery of the REE minerals and its geological significance in the Quyang bauxite deposit, West Guangxi, China. J. Asian Earth Sci. 39, 701–771. https://doi.org/10.1016/j.jseaes.2010.05.005.

Yang, M., Liang, X., Ma, L., Huang, J., He, H., Zhu, J., 2019. Adsorption of REEs on kaolinite and halloysite: a link to the REE distribution on clays in the weathering crust of granite. Chem. Geol. 525, 210–217. https://doi.org/10.1016/j.chemgeo.2019.07.024.

Yang, S.J., Wang, Q.F., Deng, J., Wang, Y.Z., Kang, W., Liu, X.F., Li, Z.M., 2019. Genesis of karst bauxite-bearing sequences in Baofeng, Henan (China), and the distribution of critical metals. Ore Geol. Rev. 115, 103–161. https://doi.org/10.1016/j.oregeorev.2019.103161.

Yusoff, Z.M., Ngwenya, B.T., Parsons, I., 2013. Mobility and fractionation of REEs during deep weathering of geochemically contrasting granites in a tropical setting, Malaysia. Chem. Geol. 349, 71–86. https://doi.org/10.1016/j.chemgeo.2013.04.016.

Yuste, A., Bauluz, B., Mayayo, M.J., 2017. Origin and geochemical evolution from ferrallitized clays to karst bauxite: an example from the lower cretaceous of NE Spain. Ore Geol. Rev. 84, 67–79. https://doi.org/10.1016/j.oregeorev.2016.12.025.

Yuste, A., Camacho, I., Bauluz, B., Mayayo, M.J., Laita, E., 2020. Palaeoweathering events recorded on siliciclastic continental deposits (Albian, Lower Cretaceous) in NE Spain. Appl. Clay Sci. 190, 105598 https://doi.org/10.1016/j.clay.2020.105598.